

# Nanoscale

Accepted Manuscript



This is an *Accepted Manuscript*, which has been through the Royal Society of Chemistry peer review process and has been accepted for publication.

*Accepted Manuscripts* are published online shortly after acceptance, before technical editing, formatting and proof reading. Using this free service, authors can make their results available to the community, in citable form, before we publish the edited article. We will replace this *Accepted Manuscript* with the edited and formatted *Advance Article* as soon as it is available.

You can find more information about *Accepted Manuscripts* in the [Information for Authors](#).

Please note that technical editing may introduce minor changes to the text and/or graphics, which may alter content. The journal's standard [Terms & Conditions](#) and the [Ethical guidelines](#) still apply. In no event shall the Royal Society of Chemistry be held responsible for any errors or omissions in this *Accepted Manuscript* or any consequences arising from the use of any information it contains.

## ARTICLE

# Morphology-tunable Synthesis of ZnO Nanoforest and its Photoelectrochemical Performance

Cite this: DOI: 10.1039/x0xx00000x

Xing Sun,<sup>a,#</sup> Qiang Li,<sup>a,b,#</sup> Jiechao Jiang<sup>c</sup> and Yuanbing Mao<sup>a,\*</sup>Received 00th January 2014,  
Accepted 00th January 2014

DOI: 10.1039/x0xx00000x

[www.rsc.org/](http://www.rsc.org/)

Understanding and manipulating the synthesis reaction and crystal growth mechanism are keys to designing and constructing the morphology and functional properties of advanced materials. Herein the morphology-controlled synthesis of three-dimensional (3D) ZnO nanoforests is reported via a facile hydrothermal route. Specifically, it is systematically studied that the respective and synergistic influence of polyethylenimine (PEI) and ammonia on the architecture of ZnO nanoforests. The in-depth understanding of mechanism of hydrothermal growth is vital for advancing this facile approach and controlling over special 3D nanostructures into versatile nanomanufacturing. More importantly, the unique architecture characteristics endow the willow-like ZnO nanoforest prominent photoelectrochemical water splitting performances, including small charge transfer resistance, long photoelectron lifetime, high photocurrent density of 0.919 mA cm<sup>-2</sup> at +1.2 V (*vs.* Ag/AgCl), and more importantly, high photoconversion efficiency of 0.299% at 0.89 V (*vs.* RHE), which leads the realm of homogeneous ZnO nanostructures. In all, it is expected that this work will open up an unprecedented avenue to govern desirable 3D ZnO nanostructures, and broadens the application potentials of 3D nanotechnology.

## 1. Introduction

Rational design and control over the morphology and function of inorganic crystals is a long-standing goal in materials science and engineering.<sup>1</sup> Various nanostructures with desirable morphologies have attracted broad attention because of their fantastic interior architectures and variation in the physicochemical properties caused by interfacial effects. These features play pivotal roles in determining nanomaterials' properties and can lead to many potential applications. Therefore, morphology-programmed and controlled synthesis with a predictive model based on morphology-property relationship will greatly advance materials science and nanotechnology while it remains as a significant challenge and in an urgent need.<sup>2-5</sup>

At the meantime, sunlight is an abundant, inexpensive, pollution-free and endlessly renewable source of clean energy. Converting solar energy into an easily usable form has attracted considerable interest in the last several decades. Among different technologies for solar energy conversion, photoelectrolysis has been used to split water into hydrogen and oxygen without any emission of byproducts. However, the conversion efficiency today remains low (*e.g.* lower than that of photovoltaics), and is limited mainly by the low performance of the photoelectrodes. To develop better photoelectrodes and more efficient devices, one of the main

strategies is the nanostructuring strategy by exploiting scaling laws and specific effects at the nanoscale to enhance the efficiency of existing semiconductors and metal oxides. This has gained significant interest in last twenty years.<sup>5</sup>

Among existing semiconductors and metal oxides, zinc oxide (ZnO) has been one of the most favorable materials. It has been widely applied in electronics, sensors, catalysts, and more recently energy conversion/storage devices due to its excellent stability, environmental friendliness and low cost.<sup>6-12</sup> Therefore, morphology-tunable synthesis of ZnO nanostructures is substantially crucial for exploring their further potentials and for enabling scientists with great manipulation power on material and device performance.<sup>4, 13, 14</sup> There are manifold synthesis methods reported in the literature for ZnO nanostructures, including hydrothermal synthesis,<sup>8, 15, 16</sup> vapor-liquid-solid (VLS) process,<sup>14</sup> chemical vapor deposition (CVD),<sup>17</sup> and microwave irradiation synthesis.<sup>13</sup> Among these well-accepted growth strategies, hydrothermal synthesis stands out and has successfully promoted bottom-up nanoscience to a new level due to its low cost, low synthesis temperature, easy scaling up, and environmental benignity.<sup>18</sup> Through introducing and altering different capping agents with preferential binding abilities on different ZnO crystal surfaces, hydrothermal synthesis possesses the capability to systematically manipulate and creatively grow ZnO nanostructures into diverse forms, such as nanorods, nanowires,

nanotubes, nanoflowers, and nanotrees.<sup>7, 8, 15, 19-22</sup> On the long list of its splendid architectures, one-dimensional (1D) ZnO nanowire arrays were considered as one of the most significant morphologies.<sup>7, 23</sup> Also, numerous reports have studied the morphology-controlled growth of ZnO nanowire arrays through hydrothermal method by exploring the dependence between shape transition of its nanowire arrays and synthesis parameters, such as ammonia (NH<sub>3</sub>·H<sub>2</sub>O) and polyethylenimine (PEI).<sup>1, 20, 24-27</sup> Moreover, compared with 1D nanowire arrays, three-dimensional (3D) branched ZnO nanotree arrays, *i.e.* nanoforest, have recently demonstrated their more marvelous performances and promising potentials in various applications, especially energy conversion and storage.<sup>10, 21, 28-30</sup> For example, our group demonstrated that ZnO@MnO<sub>2</sub> nanoforest can generate five times higher areal capacitance than the nanowire array counterparts.<sup>10</sup> The energy conversion efficiency of dye-sensitized solar cells (DSSCs) can also be improved by about five times after branching ZnO nanowire arrays.<sup>21</sup> These surprising progresses are derived from the fascinating 3D branched ZnO nanotree configuration, not only inheriting the advantages of nanowire arrays (*e.g.* shorter diffusion path for carrier transport), but also achieving largely augmented surface area within a given footprint. Similar to trees in the natural world by exposing sufficient surfaces of leaves and branches for effective photosynthesis, these branched nanostructures are expected to possess larger surface area to harvest solar light for photoelectrochemical (PEC) and photocatalytic water splitting. They also cause increased scattering to improve light absorption. Moreover, they inherit the advantages of nanostructures, such as shortened carrier collection pathways, surface area-enhanced charge transfer, potential determining ions, and quantum size confinement among others.<sup>31</sup> However, there is no report yet in the literature on how to fine tune and control the morphology of 3D ZnO nanotree arrays via engineering the hydrothermal synthesis parameters. This limits our capability to regulate and design complex 3D configurations via hydrothermal approach.<sup>32</sup> It is extremely critical for advancing this powerful fabrication approach into a versatile nanomanufacturing technology. Therefore, in-depth investigation of shape-evolution of 3D ZnO nanoforests via hydrothermal growth is urgently desired. Furthermore, 3D homogeneous ZnO nanoforests have not been explored as photoanodes in PEC cells for hydrogen generation from water splitting despite their aforementioned successful demonstrations in supercapacitors and DSSCs.<sup>10, 21</sup> To fill these voids, our group conducted morphology-programmed hydrothermal synthesis to fabricate 3D branched nanotree arrays with well-defined shape and size. The main significance of this research for tailoring the morphology and size of 3D branched ZnO nanotree arrays is to adjust the hydrolysis rate, nucleation speed, and supersaturation degree of zinc ions by controlling the potential of hydrogen (pH) value and aggregation of surfactant in the reaction solution, more specifically, the concentration of ammonia and/or PEI. Other than offering a highly enhanced surface area on limited footprint, the as-fabricated ZnO nanoforest also builds a 3D interconnected matrix structure with shorten carrier collection pathways, good electrical conductivity, and improved light absorption, which are proved to substantially benefit the PEC performance. From our measurements, the willow-like nanoforests led in PEC water splitting performance, and brush-like nanoforests surpassed nanowire arrays. Therefore, this work contributes to both scientific and technological fields because this economical low temperature fabrication technique holds extraordinary significances for large-scale solution processing of 3D hierarchical nanostructures, and the resulting nanoforest is expected to inspire a new general paradigm for various energy related applications.<sup>33</sup>

## 2. Experimental

### 2.1 Growth of ZnO Nanowire Arrays

As we previously reported, a seed solution of ZnO nanoparticles (Fig. S1†) was prepared by adding 25 mL of 0.03 M sodium hydroxide (NaOH) ethanol solution into 37.5 mL of 0.01 M zinc acetate [Zn(O<sub>2</sub>CCH<sub>3</sub>)<sub>2</sub>·2H<sub>2</sub>O] ethanol solution drop by drop, and then the mixture was actively stirred at 60 °C for 2 h.<sup>10</sup> After that, the seed solution was drop casted onto indium tin oxide (ITO) glass substrates. ZnO nanowire arrays were grown from the ZnO nanoparticle seeds through immersing in an aqueous precursor solution consisting of 0.025 M zinc nitrate hydrate [Zn(NO<sub>3</sub>)<sub>2</sub>·6H<sub>2</sub>O], 0.025 M hexamethylenetetramine (C<sub>6</sub>H<sub>12</sub>N<sub>4</sub>, HMTA), 0.05 M ammonia, and 0.0035 M PEI and heated at 60-90 °C for 7 h. The grown ZnO nanowire arrays were thoroughly rinsed with deionized water, and then dried in air (Fig. S2†).

### 2.2 Growth of ZnO Nanobranches onto the Preformed ZnO Nanowire Arrays

To develop the desirable 3D ZnO nanoforests, ZnO nanoparticle seed solution was deposited onto the surface of the preformed ZnO nanowire arrays by a similar drop casting process, and subsequently a similar hydrothermal reaction was conducted as described above. To fine tune the growth of different ZnO branches onto the ZnO nanowire array trunk, the concentrations of ammonia and PEI were varied and controlled (Table 1). To remove residual organics (mostly PEI), the as-prepared ZnO nanostructures were annealed at 350 °C in air for 10 min. After annealing, they were also ensured excellent electrical conductivity, mechanical stability, and firm adherence onto the ITO substrate.<sup>34</sup>

**Table 1.** Various PEI and ammonia concentrations used to control the growth of ZnO nanobranches onto the preformed ZnO nanowire arrays while keeping other growth conditions the same: 0.025 M Zn(NO<sub>3</sub>)<sub>2</sub>, 0.025 M HMTA, and at 60-90 °C for 3-5 hours.

Sample	[NH <sub>3</sub> ·H <sub>2</sub> O] [mol L <sup>-1</sup> ]	[PEI] [mol L <sup>-1</sup> ]
Control	0	0
Effect of [PEI]	HA1	0.03
	HA2	0.05
	HA3	0.10
	HA4	0.12
	HA5	0.15
Effect of [NH <sub>3</sub> ·H <sub>2</sub> O]	HP1	0.0035
	HP2	0.0050
	HP3	0.0070
Synergistic effect of [PEI] and [NH <sub>3</sub> ·H <sub>2</sub> O]	HAP1	0.0035
	HAP2	0.0050
	HAP3	0.0070

### 2.3 Characterization

The morphology, chemical composition, and crystal structure of the seeded substrate, as-prepared ZnO nanowire arrays and nanoforests were characterized through atomic force microscopy (AFM), scanning electron microscopy (SEM), powder X-ray diffraction (XRD), Raman spectroscopy, transmission electron microscopy (TEM), high-resolution TEM (HRTEM), selected area electron diffraction (SAED) and energy dispersive X-ray spectroscopy (EDS). AFM images of seeded substrate were taken with a Dimension 3000 AFM on TMC VT102 vibration isolation table at tapping mode. XRD analysis of the as-prepared ZnO nanoarchitectures was carried out using a Bruker AXS D8 QUEST diffractometer with Cu K<sub>α</sub> radiation ( $\lambda = 1.5406 \text{ \AA}$ ) between 25° and

70°. Raman spectroscopy was conducted on a Bruker SENTERRA RAMAN microscope with a 785 nm laser as the excitation source. XRD, Raman and SEM measurements were conducted directly with the as-prepared ZnO nanostructures on the ITO substrate. For SEM imaging, the ITO glass substrate with as-prepared ZnO nanostructures were attached directly onto the surface of SEM brass stub through conductive carbon tape using a Carl Zeiss Sigma VP Field-Emission SEM at 2-5 kV. TEM, HRTEM, SAED and EDS were carried out on a Hitachi H-9500 microscope with an accelerating voltage of 300 kV. Specimens for these studies were prepared by sonicating the as-prepared ZnO nanoforest on the ITO substrate in deionized water, followed by depositing a drop of the obtained suspension onto a 300 mesh Cu grid, coated with a lacey carbon film.

## 2.4 Optical Testing

The transmittance ( $T$ , %) and reflectance ( $R$ , %) of the three types of ZnO nanostructured samples, i.e. nanowire arrays, brush-like and willow-like nanoforests, were measured via a spectrophotometer (Lambda 950 UV/Vis/NIR, Perkin-Elmer) over the wavelength range of 200-800 nm. The absorption plus scattering ( $A + S$ , %) were calculated according to the formula  $A + S = 100 - T - R$ .

## 2.5 Photoelectrochemical Testing

PEC measurements for water splitting were performed in a standard three-electrode electrochemical cell configuration, using the as-prepared ZnO nanoarchitectures grown on ITO glass as the working electrode, a platinum wire as the counter electrode, and Ag/AgCl as the reference electrode. A 0.5 M  $\text{Na}_2\text{SO}_4$  solution buffered to pH  $\sim 7.0$  with phosphate buffer solution was employed as the electrolyte and purged with  $\text{N}_2$  for 5-10 min before the measurements. The PEC measurements, electrochemical impedance measurements, and open circuit voltage decay were recorded under AM 1.5 G illumination from a solar simulator (1 sun,  $100 \text{ mV cm}^{-2}$ , Iwasaki Solar Simulation Evaluation Systems equipped with EYE/Iwasaki electronic ballast system). The potential was measured against an Ag/AgCl reference and converted to reversible hydrogen electrode (RHE) potential by using the equation  $E(\text{RHE}) = E(\text{Ag/AgCl}) + 0.1976(\text{V}) + 0.059 \times \text{pH}$ .<sup>35</sup> All the PEC measurements were tested with illumination from the front side of the ITO glass substrate covered with the ZnO nanostructures. For each type of samples, tests were performed in triplicates in order to exclude the accidental phenomenon and prove reproducibility. Results from each type of samples agreed with each other.

## 3. Results and Discussion

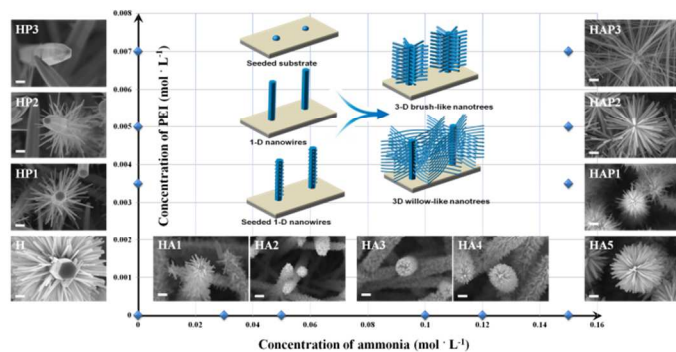


**Fig. 1** Illustration of the morphology and size evolutions of the ZnO nanobranches onto the preformed ZnO nanowire arrays to form the ZnO nanoforest by altering ammonia and PEI concentrations of the nutrient solution during the branch growth process.

Both the respective and synergistic influences of ammonia and PEI concentrations were systematically investigated on the morphology and size evolution of ZnO nanobranches onto the preformed ZnO nanowire arrays to form the ZnO nanoforest (Fig. 1).

## 2.1 Effect of Ammonia Concentration on the ZnO Branch Growth to Form ZnO Nanoforest

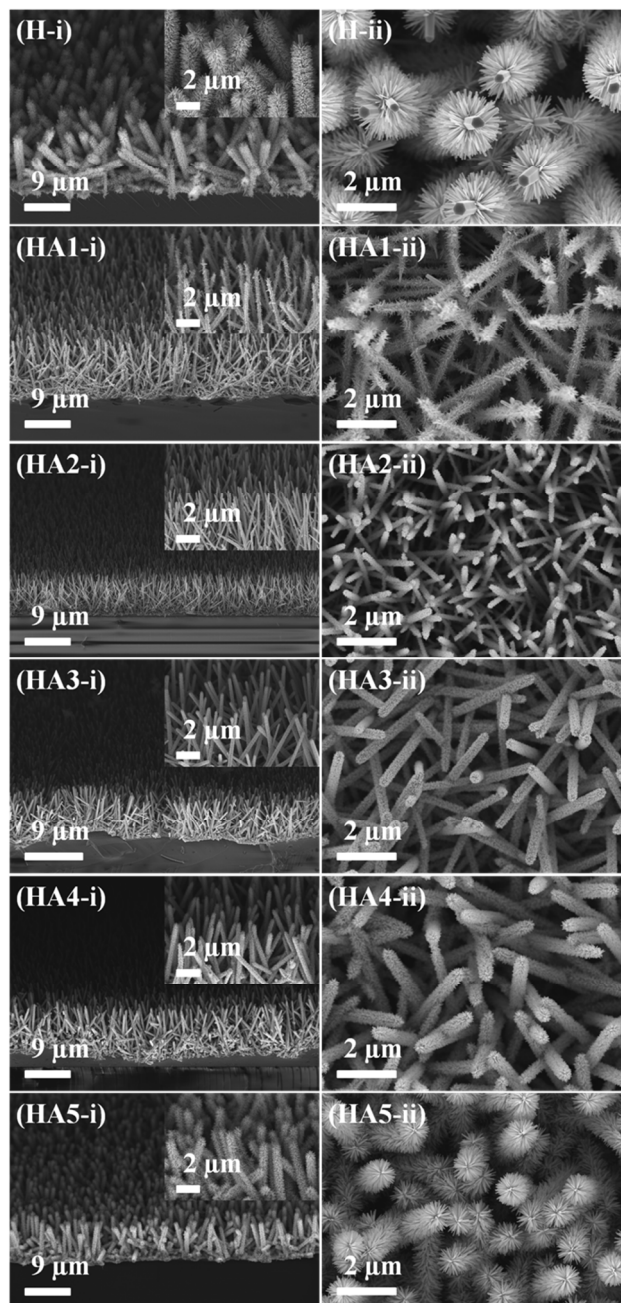


**Fig. 2** SEM images of the obtained ZnO nanoforests after growing ZnO nanobranches onto the preformed ZnO nanowire arrays in precursor solutions with different concentrations of ammonia but without PEI. H:  $c(\text{NH}_3 \cdot \text{H}_2\text{O}) = 0$ ; HA1:  $c(\text{NH}_3 \cdot \text{H}_2\text{O}) = 0.03 \text{ M}$ ; HA2:  $c(\text{NH}_3 \cdot \text{H}_2\text{O}) = 0.05 \text{ M}$ ; HA3:  $c(\text{NH}_3 \cdot \text{H}_2\text{O}) = 0.10 \text{ M}$ ; HA4:  $c(\text{NH}_3 \cdot \text{H}_2\text{O}) = 0.12 \text{ M}$ ; and HA5:  $c(\text{NH}_3 \cdot \text{H}_2\text{O}) = 0.15 \text{ M}$ . Panels (i) and (ii) represent side- and top-viewed SEM images with different magnifications.

First, to understand how the preformed ZnO nanowire arrays transform and the ZnO nanobranches evolve under the influence of ammonia addition with different concentrations, the obtained ZnO

nanostructures were studied using SEM (Fig. 2) and XRD (Fig. 3). The top- and side-viewed SEM images all clearly exhibit uniform ZnO nanoforests on large area with some changes on the ZnO trunks and branch lengths (Fig. S3A). These nanoforests are composed of oriented nanotrees uniformly rooted on the ITO glass substrate. Each of the trees consists of an upstanding trunk/stem and myriad side branches.

Under closer look, these nanoforests prepared with different ammonia concentrations have different morphologies. ZnO nanoforest was also prepared from the preformed ZnO nanowire arrays without adding ammonia and PEI in the nutrient  $\text{Zn}(\text{NO}_3)_2$  and HMTA solution for comparison. As shown in Fig. 2H, the hexagonal shape and diameter ( $\sim 200$  nm) of the ZnO nanowire trunk were kept the same after the branch growth under this condition. Relatively dense branches with a length of  $\sim 650 \pm 50$  nm grew out along the ZnO nanowire trunk. After introducing 0.03M ammonia into the nutrient solution, all branches became shorter ( $\sim 180$  nm) and the trunk top was thinned (Fig. 2HA1). With 0.05 M of ammonia, the average branch length was further shortened to  $\sim 50$  nm and the tip of the trunk was barely observed due to the coverage by the short branches (Fig. 2HA2). However, the ZnO branch growth changed when the ammonia concentration in precursor solution was kept increasing. With the ammonia concentration was equal to 0.10 M, both the diameter and length of the ZnO nanobranches started to increase (Fig. 2HA3). The petal-like branches are now  $\sim 90$  nm long and compactly wrapped all over the trunks. With even higher ammonia concentration (*i.e.* 0.15 M), the branches were prolonged to  $\sim 300$  nm (Fig. 2HA5).

Fig. 3A shows the corresponding XRD patterns of ZnO nanoforests synthesized in nutrient solutions with different ammonia concentrations. All the diffraction peaks can be easily assigned to hexagonal wurtzite ZnO (JCPDS Card No. 36-1451) without any impure peaks, which is consistent with the Raman data (Fig. S2D†). The peak positions are the same as the XRD pattern taken from the ZnO nanowire arrays before growing the ZnO branches (Fig. S2A). As shown in Fig. S2, the trunk of these ZnO nanoforests, *i.e.* the ZnO nanowire arrays, grow vertically from the ITO substrate along the direction of *c*-axis, so their strongest peak is the 0002 diffraction. For the ZnO nanoforest samples from H to HA5, their relative XRD peak intensities vary due to the altered ammonia concentration. In Fig. 3A, the peak intensities of (10 $\bar{1}$ 0), (10 $\bar{1}$ 1), (10 $\bar{1}$ 2), (11 $\bar{2}$ 0), (10 $\bar{1}$ 3), (11 $\bar{2}$ 2), and (20 $\bar{2}$ 1) crystal planes are compared to that of the normalized (0002). The intensities of all these peaks first decreased and then increased relatively with increasing ammonia concentration in the precursor solutions after the ZnO branch growth.

The degree of crystallographic preferred orientation was further evaluated quantitatively by calculating Harris's texture coefficient,  $T_c$ .<sup>25, 36</sup> The  $T_c$  is defined as:

$$T_c(hkl) = n \frac{I_m(hkl)/I_0(hkl)}{\sum_1^n I_m(hkl)/I_0(hkl)} \quad (1)$$

where  $I_m(hkl)$  is the measured relative intensity of the peak corresponding to the *hkl* diffraction,  $I_0(hkl)$  is the relative intensity from the same diffraction in the standard powder sample, and  $n$  is the total number of considered diffraction peaks. The  $T_c(hkl)$  value ranges from 1 to  $n$ , corresponding to samples having a completely random orientation or a preferred (*hkl*) orientation, respectively.

In this study, diffractions of 0002, 10 $\bar{1}$ 0, and 10 $\bar{1}$ 1 ( $n = 3$ ) were chosen as plotted in Fig. 3B after calculation using equation 1.  $T_c(0002)$  increased initially and then decreased after sample HA2 with the increasing ammonia concentration. This is diametrically opposite to  $T_c(10\bar{1}0)$ , and  $T_c(10\bar{1}1)$ . More specifically,  $T_c(0002)$  for sample HA2 is calculated to be  $\sim 2.505$ , similar to that of preformed ZnO nanowire arrays ( $T_c(0002) = 2.530$ ). This is because the morphology of the HA2 nanoforest is the closest to that of the ZnO nanowire arrays (Fig. S2C), displaying the most apparent preferred

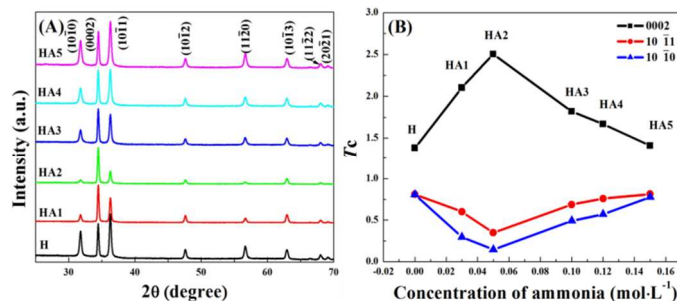


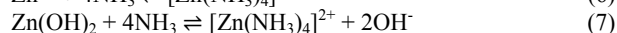
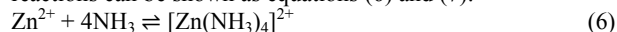
Fig. 3 (A) XRD patterns of the ZnO nanoforest samples from H to HA5. (B) Variations of the calculated Harris's texture coefficient,  $T_c$ , for 0002, 10 $\bar{1}$ 0, and 10 $\bar{1}$ 1 diffractions based on the XRD patterns shown in (A).

orientation along the  $\langle 0002 \rangle$  direction and short branches ( $\sim 50$  nm, Fig. 2HA2). While  $T_c(0002)$  values of sample H and HA5 are  $\sim 1.383$  and 1.410, respectively, which harmoniously approach the situation of random orientation with  $T_c = 1$  and are consistent with the fact of growing randomly orientated long branches onto the preformed ZnO nanowire arrays. The  $T_c$  value difference between sample H and HA5 is attributed to larger branches of the sample H, since crystalline volume can also affect the diffraction intensity.<sup>25</sup> On the other hand,  $T_c(10\bar{1}0)$  and  $T_c(10\bar{1}1)$  share similar trend with the branch length evolution from samples H to HA5 since  $T_c$  values vary as the results of both the orientation change and branch evolution of ZnO nanoforests.

Apparently, the diverse morphologies of the ZnO nanoforests were originated from different precursor solution systems. As widely reported in the literature,  $\text{Zn}(\text{NO}_3)_2$  and HMTA are the most commonly used chemical agents to hydrothermally synthesize ZnO nanostructures, including nanowires and their arrays. It is well believed that wurtzite ZnO favors inherent fast growth along the direction of its polar surfaces, and HMTA acts as a weak base and pH buffer, hydrolyzing in water and slowly releasing HCHO and  $\text{NH}_3$ .<sup>9, 37</sup> The following equations 2-5 have been proposed for the formation of oriented ZnO crystals in this type of solutions:



The addition of ammonia provides a basic environment and also mediates the heterogeneous nucleation and growth of ZnO nanostructures. In our present studies here, after 0.03 M ammonia was added into the system for sample HA1, the precursor solution immediately became turbid due to the rapid formation of white precipitate  $\text{Zn}(\text{OH})_2$  and ZnO through homogeneous nucleation. This process scrambles for free  $\text{Zn}^{2+}$  ions in the precursor solution, so the  $\text{Zn}^{2+}$  ions are depleted quickly. Under competing growth mechanisms, it leads to early termination of the heterogeneous nanobranch growth onto the seeded preformed ZnO nanowire arrays, similar to that of the nanowire array grown onto the seeded substrate. Therefore, after introducing ammonia for sample HA1 and HA2, only petals were grown onto the ZnO nanowire arrays. When the ammonia concentration reached 0.10 and 0.15 M, the precursor solutions turned clear because sufficient ammonia can coordinate with  $\text{Zn}^{2+}$  ions and generate soluble complex  $[\text{Zn}(\text{NH}_3)_4]^{2+}$ . The introduction of adequate ammonia enhances the solubility of zinc ions in the nutrient precursor solution. Less precipitation has been observed after our growth of the ZnO nanoforests. These reversible reactions can be shown as equations (6) and (7):



These  $[\text{Zn}(\text{NH}_3)_4]^{2+}$  complexes stock free  $\text{Zn}^{2+}$  ions temporarily and release them into solution through decomposition when the free  $\text{Zn}^{2+}$

ions in the solution become low/exhausted. This leads to the maintenance of a stable  $Zn^{2+}$  ion concentration and a low level of supersaturation in the system. Eventually it inhibits the homogeneous formation of ZnO and facilitates the heterogeneous growth of elongated ZnO branches onto the seeded preformed ZnO nanowire arrays.

## 2.2 Effect of PEI Concentration on the ZnO Branch Growth to Form ZnO Nanoforests

From the inspection of the PEI concentration effect on the growth of ZnO nanoforests, a fascinating phenomenon was noticed (Fig. 4). Without adding PEI and ammonia, the ZnO nanoforest trunks are all flat topped and surrounded by compact branches of  $\sim 650 \pm 50$  nm long (Fig. 2H). After adding 0.0035 M of PEI into the precursor solution, the branches grown on the preformed ZnO nanowire arrays were slim and sparse. When the PEI concentration was increased to 0.005 M, the branches became shorter ( $\sim 250$  nm long) and more sparse. The top surface of the trunks was converted into a pencil-like shape. At 0.007 M of PEI, even sharper ZnO nanowire arrays barely with branches were produced, suggesting either no branches could grow or growing branches were etched off immediately. Therefore, the highest PEI concentration used in this study was 0.007 M, because neither ZnO branches were grown on the preformed ZnO nanowire arrays (Fig. S3B) nor ZnO precipitation was formed in the solution when higher PEI concentration was introduced (data not shown).

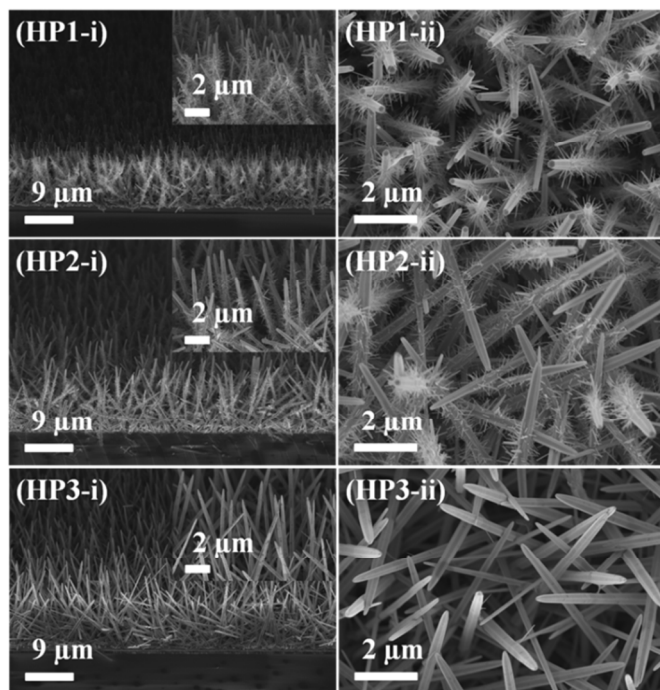


**Fig. 4** SEM images of the obtained ZnO nanoforests after growing ZnO nanobranches onto the preformed ZnO nanowire arrays in precursor solutions with no ammonia but different concentrations of PEI. HP1:  $c(\text{PEI}) = 0.0035$  M; HP2:  $c(\text{PEI}) = 0.005$  M; and HP3:  $c(\text{PEI}) = 0.007$  M.

All the peaks in the XRD patterns from the ZnO nanoforests grown with increasing PEI concentrations (Fig. 5A) can also be easily indexed to hexagonal wurtzite ZnO (JCPDS Card No. 36-1451) with no impurity peaks. The relative  $(10\bar{1}0)$ ,  $(10\bar{1}1)$ ,  $(10\bar{1}2)$ ,  $(11\bar{2}0)$ ,  $(10\bar{1}3)$ ,  $(11\bar{2}2)$ , and  $(20\bar{2}1)$  peak intensities did not fluctuate following the same trend as the branch length variation. From sample H to HP1, etching of the trunks and branches resulted

enhanced  $T_c(0002)$  and decreased  $T_c(10\bar{1}0)$  and  $T_c(10\bar{1}1)$ . From samples HP1 to HP2 and HP3,  $T_c(10\bar{1}0)$  and  $T_c(10\bar{1}1)$  were surprisingly increased with continuously trimmed branches, while  $T_c(0002)$  decreased.

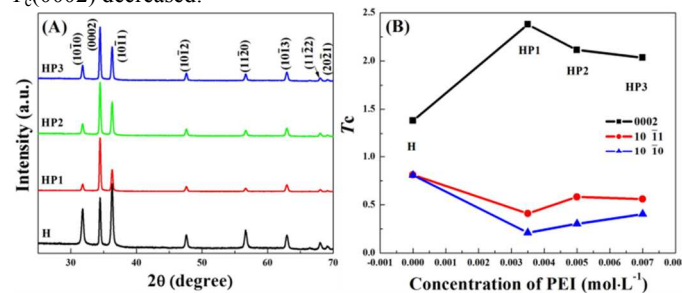
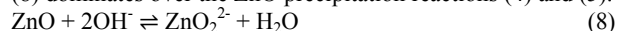


**Fig. 5** (A) XRD patterns of samples H, HP1, HP2 and HP3. (B) Variations of the calculated Harris's texture coefficient,  $T_c$ , for 0002,  $10\bar{1}0$ , and  $10\bar{1}1$  diffractions based on the XRD patterns in (A).

Similar to ammonia, PEI also provides  $\text{OH}^-$  ions and raises pH value of precursor solutions. Moreover, it promotes the solubility of  $Zn^{2+}$  ions in the nutrient precursor by complexing with free  $Zn^{2+}$  ions and depressing the opportunities of free  $Zn^{2+}$  ions to combine with  $\text{OH}^-$  ions to form  $\text{Zn}(\text{OH})_2$  or ZnO precipitate.<sup>4, 9</sup> More importantly, PEI fosters the axial growth and blocks lateral growth of ZnO nanowires by selectively absorbing onto the side surfaces. So it is a common capping agent used in hydrothermal ZnO synthesis.

The reason for the phenomena observed in Fig. 4 and Fig. 5 is because PEI can trigger surface dissolution of both preformed ZnO trunks and intermediate forming ZnO branches. As previously reported,  $\text{OH}^-$  ions attracted by the polar top planes can boost the growth and also etch the top surfaces of ZnO, depending on the amount of  $\text{OH}^-$  ions.<sup>20</sup> When the amount of  $\text{OH}^-$  ions in the precursor solution is high enough after adding PEI, the ZnO erosion reaction (8) dominates over the ZnO precipitation reactions (4) and (5).



The dissolution process started from the nonpolar facets and the edge of polar surfaces of the preformed hexagonal ZnO nanowires. Therefore, the trunk of the preformed ZnO nanowires were carved into sharp pencil-like shape and the intermediate forming branches were etched away. Compared to that of the preformed ZnO nanowire arrays (Fig. S2C), the surface of the trunk nanowires became rather rough after growing ZnO nanobranches with  $c(\text{PEI}) = 0.007$  M (Fig. 4HP3) due to the erosion by extra  $\text{OH}^-$  ions. The final shape of these ZnO nanotrees reflects the balance of ZnO surface nucleation and chemical corrosion (reactions 4+5 vs 6). Similarly, the decreasing  $T_c(0002)$  is also resulted from the fact that the extra PEI and  $\text{OH}^-$  ions corroded both ZnO nanowire trunk and intermediate branches. On the other hand, both  $(10\bar{1}0)$  and  $(10\bar{1}1)$  crystal surfaces were exposed after the corrosion by  $\text{OH}^-$  ions, so the diffraction on these two planes increased, i.e. both  $T_c(10\bar{1}0)$  and  $T_c(10\bar{1}1)$  enhanced from HP1 to HP2. For HP3, higher  $T_c(10\bar{1}0)$  were observed due to more disclosed  $(10\bar{1}0)$  plane surface, while the slightly decreased  $T_c(10\bar{1}1)$  suggests the corrosion of the  $(10\bar{1}1)$  surface was slowed down. Therefore, PEI can etch the preformed hexagonal ZnO nanowires into slim and sharp shape other than modulate the growth process of ZnO nanowires/branches.

## 2.3 Synergistic Effect of Ammonia and PEI Concentrations on the ZnO Branch Growth to Form ZnO Nanoforests

As discussed above, the individual effects of ammonia and PEI on the ZnO branch growth onto the preformed nanowire arrays are quite different although they share similar characteristics, such as raising  $\text{OH}^-$  ion concentration and coordinating with  $Zn^{2+}$  ions to increase

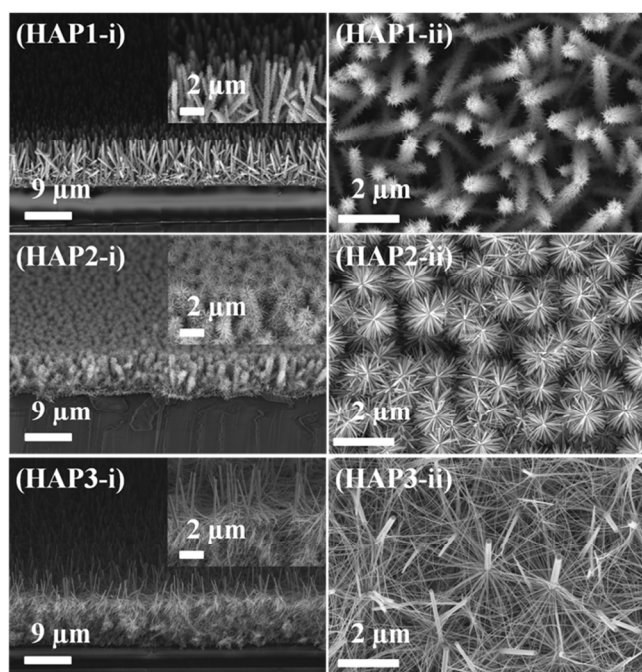
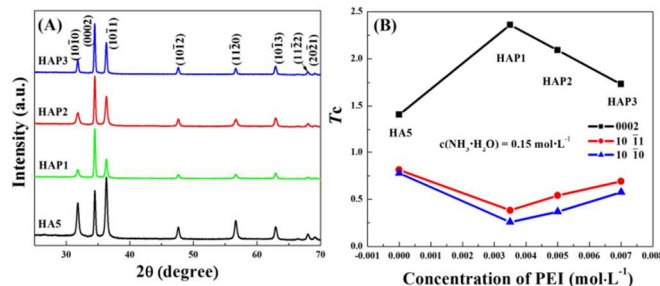


**Fig. 6** SEM images of ZnO nanoforest after growing ZnO nanobranched onto the preformed ZnO nanowire arrays from the precursor solution with 0.15 M of ammonia and varying concentrations of PEI. HAP1:  $c(\text{PEI}) = 0.0035 \text{ M}$ ; HAP2:  $c(\text{PEI}) = 0.005 \text{ M}$ ; HAP3:  $c(\text{PEI}) = 0.007 \text{ M}$ .

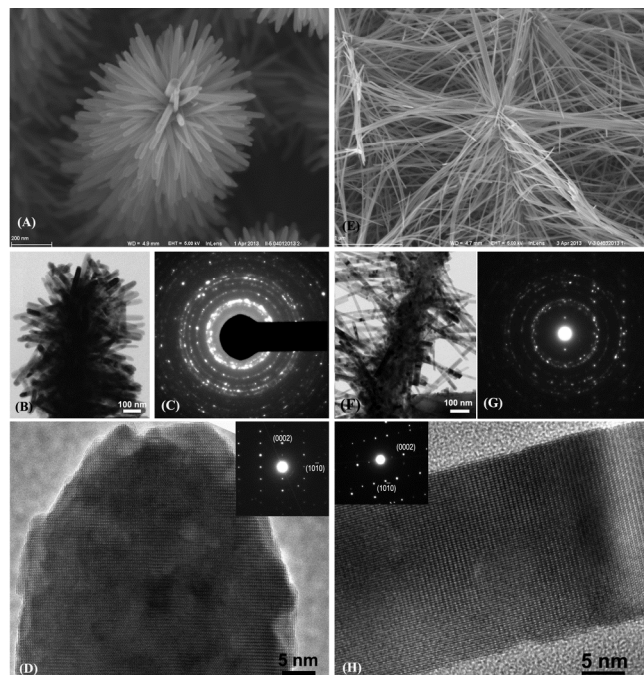
$\text{Zn}^{2+}$  solubility. To probe their synergistic influence, the concentration of PEI was chosen at 0.0035 M, 0.005 M and 0.007 M under fixed ammonia concentration of 0.15 M since the ZnO branches grew pretty long with 0.15 M ammonia and no PEI (Fig. 2HA5). As shown in Fig. 6 and Fig. S3C, the ZnO branches of sample HAP1 became sharp-ended and sparsely dispersed after adding 0.0035 M PEI into the nutrient solution with 0.15 M of ammonia. When the PEI concentration was increased to 0.005 M, the sharp-ended branches were extended from  $\sim 180 \text{ nm}$  to  $\sim 400 \text{ nm}$  (Fig. 6HAP2). With 0.15 M of ammonia and 0.007 M of PEI in the nutrient solution system, plenty of well-dispersed nanofiber-like branches were nearly perpendicularly orientated and randomly aligned along individual 6-fold planes of the preformed ZnO nanowire trunks, with aspect ratio of  $\sim 600$  ( $\sim 12 \mu\text{m}$  in length and  $\sim 20 \text{ nm}$  in diameter, Fig. 6HAP3). This is surprisingly different from the results obtained without adding ammonia, where branches hardly formed (Fig. 4HP3). These willow-like nanotree arrays construct a highly inter-connected 3D nano-matrix.<sup>28, 35, 38</sup>

XRD patterns of samples HAP1, HAP2 and HAP3 demonstrated that all these samples possess pure ZnO without any impurity phases. Also the relative  $(10\bar{1}0)$ ,  $(10\bar{1}1)$ ,  $(10\bar{1}2)$ ,  $(11\bar{2}0)$ ,  $(10\bar{1}3)$ ,  $(11\bar{2}2)$ , and  $(20\bar{2}1)$  peak intensities increase tightly associated with the branch elongation (Fig. 7A). Supported by the SEM images (Fig. 6), XRD patterns and the calculated Harris's texture coefficients  $T_c$  in Fig. 7B both demonstrated that sample HAP1 with shorter branches has more intense orientation on 0002 diffraction, which decreases from HAP1 to HAP2 and HAP3 with reducing  $T_c(0002)$ . For HAP2 and HAP3, the branches were substantially stretched and prolonged, hence the lateral  $10\bar{1}0$  and  $10\bar{1}1$  diffractions were enhanced, inducing increasing  $T_c(10\bar{1}0)$  and  $T_c(10\bar{1}1)$ . The Harris's texture coefficients of sample HA5 are different from those of samples HAP1-HAP3 due to the orientation of crystallite but also the thickness, length, and density of the ZnO branches.

The morphology and crystal structure of the as-synthesized ZnO nanoforests were also studied by TEM and HRTEM. Fig. 8A and 8B



**Fig. 7** (A) XRD patterns of samples HA5, HAP1, HAP2 and HAP3. (B) Variations of the calculated Harris's texture coefficient  $T_c$  for 0002,  $10\bar{1}0$  and  $10\bar{1}1$  diffractions based on the XRD patterns shown in (A).



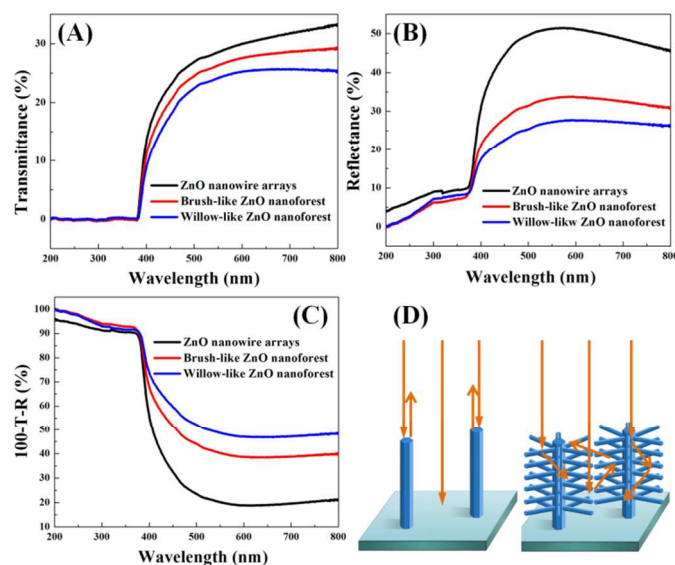
**Fig. 8** (A) SEM, (B) TEM image and (C) SAED pattern of an individual ZnO nanotree of sample HA5. (D) HRTEM image and SAED (inset) of a branch from the ZnO nanotree shown in (A-C). (E) SEM, (F) TEM image and (G) SAED pattern of a willow-like ZnO nanotree of sample HAP3. (H) HRTEM image and SAED pattern of a branch from the willow-like ZnO nanotree shown in (E-G).

exhibit representative SEM and TEM images of an individual ZnO nanotree from sample HA5, respectively. Branches were densely and randomly aligned on the preformed ZnO trunks. These branches have a diameter of  $\sim 40 \text{ nm}$ . Fig. 8C shows a SAED pattern taken from the whole nanotree shown in Fig. 8B. No significant indication of orientation preference of the branches was observed. Fig. 8D shows a typical HRTEM image of the tip of such a branch and the corresponding SAED pattern (inset). HRTEM studies and electron diffraction analysis show that all ZnO branches have a single-crystal hexagonal structure with the  $[0001]$  direction parallel to their long-axis direction. Similarly, Fig. 8E and 8F are SEM and TEM images of a typical individual willow-like nanotree of sample HAP3. Densely-stacked slim nanofiber-like branches are shown upwardly orientated, well dispersed and distributed along their preformed ZnO trunk. In Figure 8F, some branches were broken off the trunk during the ultrasonication of TEM sample preparation. Figure 8G shows a SAED pattern taken from the entire willow-like nanotree in Figure 8F exhibiting randomly oriented branches, *i.e.*, all branches do not possess the same crystallographic orientation and alignment. Figure 8H shows a typical HRTEM image and the corresponding SAED

pattern (inset) of a branch from a willow-like nanotree presenting a single-crystal hexagonal structure with the [0001] direction parallel to its long-axis direction.

After assembling all the typical SEM images of various ZnO nanotrees shown in Fig. 2, 4 and 6 into Fig. 1, the influence of the PEI and ammonia concentrations on tuning the ZnO nanotree morphology is quite evident. Low concentration ammonia etches the branches on ZnO nanotrees into petal-like structure, attributed to the competing mechanisms by producing homogeneous nuclei in solution and heterogeneous growth on the trunks after adding low amount of ammonia into the solution system. When its amount was sufficient high, ammonia coordinated with  $\text{Zn}^{2+}$  ions, assisting nucleation and growth of ZnO branches and also inhibiting the formation of homogeneous nuclei. On the other hand, PEI etched the nonpolar surfaces of ZnO nanowires, but still supported the growth on polar surfaces along *c*-axis. Surprisingly the cooperation of ammonia and PEI stretches and extends the growth of ZnO secondary branches onto the nanowire arrays substantially long and slim, forming an intertwining 3D ZnO network. Therefore, based on the interesting results discussed above, we believe that desirable architectures of 3D ZnO nanoforests can be readily designed and programmed via tailoring and engineering ammonia and PEI concentrations in nutrient solutions with the aim to control their functional properties and fulfil the demands from various potential applications, for example, photoelectrochemical water splitting discussed below, in addition to energy storage and conversion.

#### 2.4 Optical Properties of the ZnO Nanoforests



**Fig. 9** Optical characterization of ZnO nanowire arrays, brush-like ZnO nanoforest, and willow-like ZnO nanoforest grown on ITO glass: (A) Transmittance, (B) Reflectance, and (C) absorption plus scattering spectra, measured using UV-Vis spectrophotometer over a wavelength range of 200–800 nm. It is worth mentioning that  $A + S = 100 - R - T$  rather than  $A = 100 - T$  for highly rough films, to count for the loss of light transmission primarily results from reflection and scattering.<sup>39</sup> (D) Schematic illustration of interactions of light with ZnO nanowire array and nanoforest for comparison.

The optical characterizations of ZnO nanowire arrays (sample H), brush-like nanoforest (sample HA5) and willow-like nanoforest (sample HAP3) were carried out using UV-Vis spectrophotometer to reveal the light absorption features along with structural evolution. The integrated light absorption plus scattering ( $A + S$ , %) was calculated by subtracting transmittance ( $T$ , %) and reflectance ( $R$ , %) from 100% incident light. The transmittance spectra in Fig. 9A and

reflectance spectra in Fig. 9B reveal that the optical properties of the three nanostructures are very similar when the energy of excitation photons exceeds the ZnO band gap ( $\lambda < \sim 388$  nm). The ZnO nanowire arrays and two types of nanoforests absorb all incident light. The only difference is that the reflectance of the nanowire array specimen is  $\sim 4.2\%$  higher than its two nanoforest counterparts.<sup>39, 40</sup> The near/middle UV light's penetration depth of  $\sim 40$  nm is within the dimensional scales of the ZnO nanowires and nanoforests, which endows the complete light absorption by these dense nanostructures.

The major variations of light transmittance and reflectance from these three ZnO nanostructures occur within visible light region ( $400 < \lambda < 800$  nm) and can be primarily attributed to the scattering event amongst primary and secondary ZnO nanostructures. The transmittance at  $\lambda = 550$  nm through the ZnO nanowire arrays, brush-like nanoforest and willow-like nanoforest is 28.5, 26.3 and 24.1%, respectively (Fig. 9A). The decrease of  $T\%$  from these three different nanostructures can arise from the increase of surface coverage of the respective ZnO nanostructures on ITO substrates. This is in good agreement with our SEM studies (Figures 2, 4 and 6). The brush-like nanoforest specimen accommodates dense branches in the voids of primary ZnO nanowire array trunks and thus significantly increases the volume filling factor of ZnO nanowire arrays. Furthermore, the willow-like nanoforest with ultralong secondary branches forming an interconnected network further fills the non-*Z* axis space and decreases the electrode transparency and light transmission. The reflectance at  $\lambda = 550$  nm from the ZnO nanowire arrays, brush-like nanoforest and willow-like nanoforest is 51.3, 33.4 and 27.2%, respectively (Fig. 9B). This indicates more and more incident light is reflected among the dense secondary branches in a scattering mode along with evolving multi-dimensional complexity.<sup>39, 40</sup> As illustrated in Fig. 9D, when it comes to the tree-like ZnO nanostructures, multiple reflection effect increases significantly, which eventually increases light absorption and lowers light surface reflection. The multiple reflections in the nanoforests extend the light absorption path and enable more interaction sites to associate with light. Worth noting is that the willow-like ZnO nanoforest possesses fine-tuned nanobranches with comparatively high aspect ratio, so the interconnected ultralong nanobranches of the willow-like nanoforest captures and traps more incident light in comparison with those of the brush-like nanoforest. The unique structural characteristics of willow-like nanoforest result in the highest integrated light absorption plus scattering value ( $A + S$ , %) at  $\lambda = 550$  nm of 48.6%, compared to 20.2% of ZnO nanowire arrays and 40.4% of brush-like nanoforest (Fig. 9C). It should be noted that a portion of the ( $A + S$ )% would derive from the 180 nm ITO nanoparticle coating on the glass substrates as well as the surface defect states of the ZnO nanostructures while this portion should be the same from these three samples since the same ITO substrate was used. Overall, the increased volume filling factor by the multi-dimensional growth of ZnO nanowires and nanobranches plays an essential role to enhance light absorption through multiple light scattering. The precise tailoring of morphology allows effective control of ZnO nanostructures over the UV-Visible light absorption.

#### 2.5 Photoelectrochemical Water Splitting Performance of the ZnO Nanoforests

Tree-like ZnO nanowire anodes with maximized dense nanobranches have been foreseen to exhibit optimal solar cell performance, due to the nanobranches filling the space between the nanowire trunk substantially increase the surface area and act as single-crystalline charge transport pathways with shorter distance.<sup>41</sup> Our group recently demonstrated that 3D ZnO@MnO<sub>2</sub> core@shell

nanoforest electrodes for electrochemical energy storage devices offer 5 times higher areal capacitances, advanced rate capability, and better charge-discharge stability, compared with their corresponding nanowire array counterpart. Moreover, it has also demonstrated that long branched tree-like ZnO nanowire dye-sensitized solar cells (DSSCs) can raise the overall light-conversion efficiency almost 5 times compared with DSSCs constructed by upstanding ZnO nanowires. It was attributed to enlarged surface area for higher dye loading and light capture, and reduced charge recombination by providing direct conduction pathways along the crystalline ZnO nanotree multi-generation branches.<sup>21</sup> Although branched ZnO nanotetrapods as photoanodes have been employed in PEC water splitting, ZnO nanoforests have not been utilized to build a 3D interconnected conductive matrix for solar-to-hydrogen production yet.<sup>35</sup> To fill the knowledge gap and discover more potentials of ZnO nanoforests in energy conversion and storage, three typical architectures, *i.e.* ZnO nanowire arrays (sample H), brush-like nanoforest (sample HA5) and willow-like nanoforest (sample HAP3), were evaluated as photoanodes in PEC cells with the same footprint of 0.7 cm<sup>2</sup> from photoelectrochemical water splitting for hydrogen generation (Fig. 10).

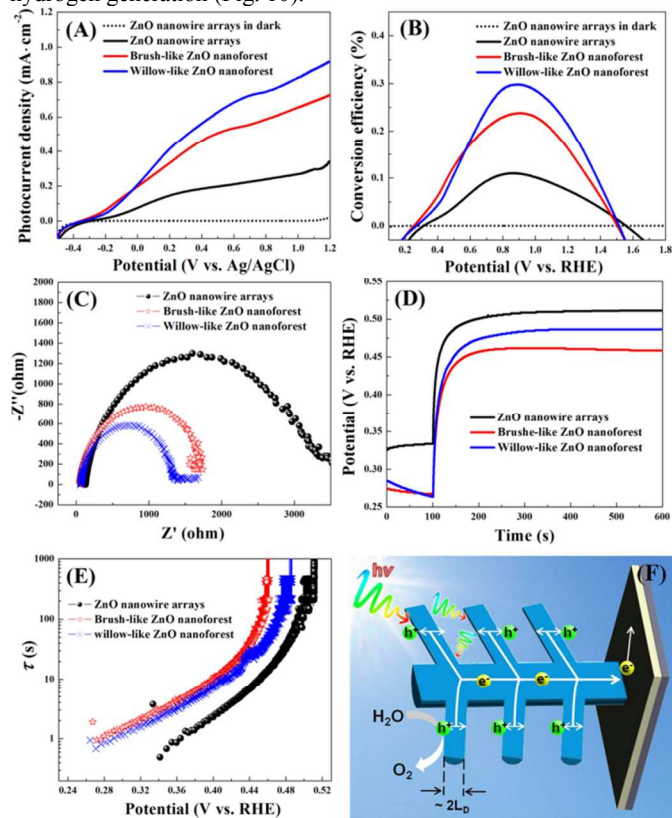


**Fig. 10** (A) Photocurrent density-potential curves; (B) photoconversion efficiency; (C) impedance spectra; (D) response of  $V_{oc}$ ; and (E) photoelectron lifetime from three nanostructured ZnO architectures: nanowire arrays, short-branched nanoforest, and willow-like nanoforest; (F) Schematic model displaying the illuminated photoanode to explain the enhanced charge transport and light trapping in willow-like ZnO nanoforest.

Fig. 10A shows the linear sweep voltammograms recorded from -0.5 to +1.2 V (*vs.* Ag/AgCl) on these three ZnO nanoarchitectures under irradiation (100 mW/cm<sup>2</sup>) as well as the nanowire arrays in the dark for comparison. The scan for the nanowire arrays in the dark displayed a negligible current density in the range of ~0.001 mA/cm<sup>2</sup>. Illuminated by the simulated solar light, the willow-like ZnO nanoforest stood out with its maximum current density of 0.919 mA/cm<sup>2</sup> at +1.2 V (*vs.* Ag/AgCl), which is more than 267% and

126% advancement in comparison with the ZnO nanowire arrays (0.344 mA/cm<sup>2</sup>) and the brush-like nanoforest (0.727 mA/cm<sup>2</sup>). Significantly, no saturation of photocurrent density was observed on these three samples at the highest measured potential, *i.e.* +1.2 V (*vs.* Ag/AgCl in this study), suggesting efficient charge separation and collection in these unique ZnO nanoarchitectures under solar irradiation. More impressively, the maximum current density achieved from our willow-like ZnO nanoforest (0.919 mA/cm<sup>2</sup> at +1.2 V *vs.* Ag/AgCl) demonstrates huge enhancement compared with those recently reported in literature, *i.e.* 765%, 644%, and 367% of branched ZnO nanotetrapods (0.12 mA/cm<sup>2</sup> at +0.31 V *vs.* Ag/AgCl),<sup>35</sup> ZnO thin film (0.1425 mA/cm<sup>2</sup> at +1.0 V *vs.* Ag/AgCl),<sup>42</sup> and ZnO nanocorals (0.25 mA/cm<sup>2</sup> at +1.2 V *vs.* RHE), respectively.<sup>43</sup>

To quantitatively evaluate the efficiency of PEC hydrogen generation from the prepared different ZnO nanoarchitectures, the photoconversion efficiency (PCE) is calculated based on the following equation:<sup>44</sup>

$$PCE = \frac{J_p}{P_0} (E_{rev}^0 - |E_b|) \quad (9)$$

where  $J_p$  is the photocurrent density (mA·cm<sup>-2</sup>);  $P_0$  is the incident light intensity (100 mW·cm<sup>-2</sup>);  $E_{rev}^0$  is the standard state-reversible potential for water splitting (1.23 eV); and  $E_b$  is the applied bias potential, which is the difference between the potential at the measuring point and the electrode open-circuit potential under the same illumination intensity. As shown in Figure 10B, the ZnO nanowire arrays achieved its highest efficiency of 0.110% at 0.85 V (*vs.* RHE), consistent with the previously reported typical value for undoped ZnO nanowire arrays.<sup>45</sup> The conversion efficiency for the brush-like nanoforest reached 0.236% at 0.85 V (*vs.* RHE). Our willow-like nanoforest distinguishes itself with photoconversion efficiency of 0.299% at 0.89 V (*vs.* RHE) from all previously reported homogeneous ZnO nanostructured photoanodes (*i.e.* pure ZnO without doping nor noble metal decoration), such as branched ZnO nanotetrapods (0.045% at +0.82 V *vs.* RHE) and 3D ZnO nanosuperstructures (0.028% at +0.98 V *vs.* RHE).<sup>35, 46</sup>

To certify that longer branches can facilitate charge migration, electrochemical impedance spectroscopy (EIS) was measured for these three typical ZnO nanoarchitectures over the frequency range of 10<sup>-2</sup>-10<sup>6</sup> Hz. The Nyquist plots (Fig. 10C) consist of one dominant semicircle, whose diameter is associated to charge transfer resistance at ZnO/electrolyte interface.<sup>2, 47</sup> With longer branches, the ZnO nanoforests exhibited smaller diameters comparing with the nanowire array counterpart, implying that the branching of nanowire arrays motivated better charge transfer. With longer and thinner ZnO branches, the willow-like nanoforest takes full advantage of space by filling the voids between nanowire trunks, and so offering minimized charge transfer resistance.

Photoelectron lifetime is associated with decay rate  $V_{oc}$  by the following equation:<sup>2, 48</sup>

$$\tau = \frac{k_B T}{e} \left( \frac{dV_{oc}}{dt} \right)^{-1} \quad (10)$$

where  $\tau$  is the photoelectron lifetime,  $k_B$  is Boltzmann's constant,  $T$  is the temperature,  $e$  is the charge of a single electron, and  $V_{oc}$  is the open-circuit voltage. With the morphology of ZnO nanoarchitectures transits from the nanowire arrays to nanoforests, the photoelectron lifetime was evidently prolonged (Fig. 10D and 10E), implying less charge trapping and more efficient charge separation. However, compared with that of the brush-like nanoforest, the photoelectron lifetime of the willow-like nanoforest was slightly reduced. Two possible reasons were hypothesized. The first one is because the fine fiber-like nanobranches with ~20 nm in diameter potentially possess more surface defects which can act as active sites for charge recombination, even though the fine nanobranches can facilitate minority carrier diffusion to electrode/electrolyte interface to

maintain more photoelectrons and holes, and increased surface area could capture and trap more sunlight accordingly. Subsequently the opportunity of charge recombination increases and the average photoelectrons lifetime are lightly decoupled. At the meantime, fiber-like branches of willow-like nanoforest reached far enough from one trunk to another via the connections between each other. However, their junctions are potential active spots where several photo-generated electrons and holes can recombine.<sup>49</sup> Even with this small drawback, the willow-like ZnO nanoforest is still not hindered from possessing decent overall PEC water splitting performance.

In the domain of homogeneous ZnO nanostructured electrodes for PEC water splitting, such unbeatable performances of willow-like nanoforests can be interpreted from the following aspects. First of all, the greatly increased surface area and roughness factors of the nanoforests result in huge photocurrent density increase, associated with efficient light and photon harvesting. Like nature trees, upstanding nanotree arrays provided straight-forward light path and long light penetration depth, avoiding the thickness limitations of densely stacked nanoparticles or thin films. The nanosized branches effectively help extend the light propagation path and improve light trapping, because of the multiple times of internal light reflection and scattering on the surface of branches.<sup>32, 39, 50</sup> As a complicated 3D maze for light, nanoforest configuration entirely quadrupled the opportunities of light-ZnO interactions (Fig. S5). It was reported that tree-like ZnO micro/nanostructures have broader absorption in solar spectrum than ZnO nanowires, because tree-like shapes can activate maximized excitonic band gaps of wurtzite ZnO.<sup>51</sup> Thus, resulting from large surface area and high light-trapping capability, the charge generation efficiency was greatly improved.

To elucidate the superiority of our ZnO nanoforest photoanodes, the mechanism of charge transport have also been carefully considered. As illustrated in Fig. 10F, under irradiation, photo-generated electron and hole pairs on the ZnO photoanode split water (H<sub>2</sub>O) molecules into gaseous oxygen (O<sub>2</sub>), hydrogen ions (H<sup>+</sup>), and electrons at the ZnO/electrolyte interface. Gaseous O<sub>2</sub> molecules are created at the anode and H<sup>+</sup> ions migrate to the cathode through electrolyte. Meanwhile, the photoelectrons flow to the cathode through external circuit and reduce H<sup>+</sup> ions into gaseous hydrogen (H<sub>2</sub>). The efficiency of photoanode predominantly relies on slowing down or even eliminating the electron-hole recombination and improving charge transport properties in the electrolyte/photoanode/back electrode configuration.<sup>52</sup> Our ZnO nanoforests have densely packed ultrathin branches, especially the fiber-like branches of the willow-like nanoforest with diameter of ~20 nm (Fig. 6HAP3 and Fig. 8D-H), which efficiently shrink the diffusion length ( $L_D$ ) of holes and prevent carrier recombination.<sup>23</sup> The willow-like nanoforest with the lowest charge transfer resistance was ascertained by EIS data in Fig. 10C. In addition, the well crystallized ZnO branches and trunks facilitated electron transportation as conductive and directional highway, especially along their *c*-axis, several orders of magnitude faster than those densely packed nanoparticles.<sup>49</sup> All those factors expedite the charge separation, the transportation of holes to the ZnO/electrolyte interface for water oxidation, and the delivery of photoelectrons to the current collector on the back, minimize of recombination probabilities of photocarriers and optimize charge transfer kinetics.

The third consideration is charge collection efficiency, which is associated with the interfacial surface area and the connection between the ZnO nanoforest photoanode and ITO substrate. The large surface area of the ZnO nanoforest induce a full contact and a rapid delivery of holes from reaction sites to water, facilitating the hole transfer kinetics at ZnO/electrolyte interface and boosting collection efficiency of holes. Moreover, like nature trees delivering water and carbohydrates, our dendritic ZnO nanotrees optimize

efficient photoelectron collection from myriad terminals to the central trunks, which are tightly rooted on the current collector. Hence, the unique geometry of our ZnO nanoforests provides high surface area without sacrificing electron transportation and collection, and ensures efficient charge collection efficiency.

This work manipulated the principle of morphological modulation for 3D ZnO nanoforests by tuning the concentrations of ammonia and PEI (therefore, their relative ratio). The generated nanoarchitectures, specifically the willow-like ZnO nanoforest, harvest solar light efficiently and deliver excellent PEC water splitting performance. The unique geometry of our ZnO nanoforests guarantees high efficiency in charge generation, transportation, and collection processes. Therefore they outperform all other homogeneous ZnO photoanodes in terms of PEC water splitting for hydrogen generation. This type of nanoarchitectures is also highly expected to outperform other morphologies in various energy conversion and storage devices, such as solar cells and batteries. On the other side, an Achilles' heel of the pure ZnO nanoforest is that they are still not able to capture visible light in the solar spectrum, restricted inherently by large band gap of ZnO.<sup>53, 54</sup> It is believed that this drawback can be tackled by substitutional doping, decorating with noble metal, sensitizing or integrating into core/shell heterogeneous nanostructures.<sup>44, 53-60</sup> Therefore, the as-prepared ZnO nanoforest reported here are qualified to be an ideal photo-active matrix material.

## Conclusions

In summary, unique 3D ZnO nanoforests have been successfully synthesized via a facile hydrothermal process of ZnO nanobranches onto preformed ZnO nanowire arrays. The morphology of the 3D ZnO nanotrees was tailored by symmetrically tuning the PEI and ammonia concentrations, which mediate the surface chemistry and shape the directional growth of the ZnO crystalline nanobranches onto the preformed ZnO nanowire arrays. The obtained unique nanoarchitecture endows the willow-like ZnO nanoforest prominent PEC water splitting performances, including small charge transfer resistance, long photoelectron lifetime, high photocurrent density of 0.919 mA cm<sup>-2</sup> at +1.2 V (vs. Ag/AgCl) and photoconversion efficiency (0.299% at 0.89 V (vs. RHE), which leads the realm of homogeneous ZnO nanostructures. Therefore, this work opens up a promising avenue by governing desirable 3D ZnO nanostructures based on demands, and broadens the application potentials of 3D nanotechnology to both minimized functional and large-scale industry devices. Moreover, it is expected that these 3D ZnO nanoforests will make more innovations in the field of PEC hydrogen production in conjunction with doping and decoration, and benefit the entire energy storage and conversion field.

## Acknowledgements

The authors thank the support from the University of Texas-Pan American (startup for YM), American Chemical Society - Petroleum Research Fund #51497 (YM), the Welch Foundation (BG-0017), and the National Science Foundation under DMR grant # 0934157 (PREM-UTPA/UMN-Science and Engineering of Polymeric and Nanoparticle-based Materials for Electronic and Structural Applications) and DMR MRI grant #1040419.

## Notes and references

<sup>a</sup>Department of Chemistry, The University of Texas - Pan American, Edinburg, TX 78539 USA

<sup>b</sup>Department of Mechanical Engineering, The University of Texas - Pan American, Edinburg, TX 78539 USA

<sup>c</sup>Materials Science and Engineering Department, The University of Texas at Arlington, Arlington, TX, 76019 USA

<sup>#</sup>Both authors contributed equally to this work

<sup>\*</sup>To whom correspondence should be addressed: Phone: +1 956 665 2417; Fax: +1 956 665 5006; E-mail: maoy@utpa.edu

<sup>†</sup>Electronic Supplementary Information (ESI) available: supplementary figures. See DOI: 10.1039/b000000x/

1. J. Joo, B. Y. Chow, M. Prakash, E. S. Boyden and J. M. Jacobson, *Nat. Mater.*, 2011, 10, 596-601.
2. M. Zhou, H. B. Wu, J. Bao, L. Liang, X. W. Lou and Y. Xie, *Angew. Chem. Int. Ed. Engl.*, 2013, 52, 8579-8583.
3. Z. Q. Sun, J. H. Kim, Y. Zhao, F. Bijarbooneh, V. Malgras, Y. Lee, Y. M. Kang and S. X. Dou, *J. Am. Chem. Soc.*, 2011, 133, 19314-19317.
4. T. L. Sounart, J. Liu, J. A. Voigt, M. Huo, E. D. Spoeke and B. McKenzie, *J. Am. Chem. Soc.*, 2007, 129, 15786-15793.
5. S. C. Warren, K. Voitchovsky, H. Dotan, C. M. Leroy, M. Cornuz, F. Stellacci, C. Hebert, A. Rothschild and M. Gratzel, *Nat. Mater.*, 2013, 12, 842-849.
6. T. R. Zhang, W. J. Dong, M. Keeter-Brewer, S. Konar, R. N. Njabon and Z. R. Tian, *J. Am. Chem. Soc.*, 2006, 128, 10960-10968.
7. Z. L. Wang, *MRS Bull.*, 2012, 37, 814-827.
8. R. Kozhummal, Y. Yang, F. Guder, A. Hartel, X. L. Lu, U. M. Kucukbayrak, A. Mateo-Alonso, M. Elwenspoek and M. Zacharias, *ACS Nano*, 2012, 6, 7133-7141.
9. S. Xu and Z. L. Wang, *Nano Res*, 2011, 4, 1013-1098.
10. X. Sun, Q. Li, Y. Lu and Y. Mao, *Chem. Commun.*, 2013, 49, 4456-4458.
11. Z. L. Wang, R. Guo, L. X. Ding, Y. X. Tong and G. R. Li, *Sci. Rep.*, 2013, 3, 1204.
12. Q. Kuang, Z. Y. Jiang, Z. X. Xie, S. C. Lin, Z. W. Lin, S. Y. Xie, R. B. Huang and L. S. Zheng, *J. Am. Chem. Soc.*, 2005, 127, 11777-11784.
13. S. Cho, S. H. Jung and K. H. Lee, *J. Phys. Chem. C*, 2008, 112, 12769-12776.
14. J. Shi, H. Hong, Y. Ding, Y. A. Yang, F. Wang, W. B. Cai and X. D. Wang, *J. Mater. Chem.*, 2011, 21, 9000-9008.
15. W. W. Lee, J. Yi, S. B. Kim, Y. H. Kim, H. G. Park and W. I. Park, *Cryst. Growth Des.*, 2011, 11, 4927-4932.
16. C. W. Cheng, B. Liu, H. Y. Yang, W. W. Zhou, L. Sun, R. Chen, S. F. Yu, J. X. Zhang, H. Gong, H. D. Sun and H. J. Fan, *ACS Nano*, 2009, 3, 3069-3076.
17. H. S. Song, W. J. Zhang, C. Cheng, Y. B. Tang, L. B. Luo, X. Chen, C. Y. Luan, X. M. Meng, J. A. Zapien, N. Wang, C. S. Lee, I. Bello and S. T. Lee, *Cryst. Growth Des.*, 2011, 11, 147-153.
18. W. D. Shi, S. Y. Song and H. J. Zhang, *Chem. Soc. Rev.*, 2013, 42, 5714-5743.
19. Z. R. R. Tian, J. A. Voigt, J. Liu, B. McKenzie, M. J. McDermott, M. A. Rodriguez, H. Konishi and H. F. Xu, *Nat. Mater.*, 2003, 2, 821-826.
20. K. S. Kim, H. Jeong, M. S. Jeong and G. Y. Jung, *Adv. Funct. Mater.*, 2010, 20, 3055-3063.
21. S. H. Ko, D. Lee, H. W. Kang, K. H. Nam, J. Y. Yeo, S. J. Hong, C. P. Grigoropoulos and H. J. Sung, *Nano Lett.*, 2011, 11, 666-671.
22. F. H. Zhao, J. G. Zheng, X. F. Yang, X. Y. Li, J. Wang, F. L. Zhao, K. S. Wong, C. L. Liang and M. M. Wu, *Nanoscale*, 2010, 2, 1674-1683.
23. A. Soudi, P. Dhakal and Y. Gu, *Appl. Phys. Lett.*, 2010, 96, 253115.
24. K. F. Liu, W. B. Wu, B. L. Chen, X. D. Chen and N. N. Zhang, *Nanoscale*, 2013, 5, 5986-5993.
25. T. Shinagawa, S. Watase and M. Izaki, *Cryst. Growth Des.*, 2011, 11, 5533-5539.
26. M. Law, L. E. Greene, J. C. Johnson, R. Saykally and P. D. Yang, *Nat. Mater.*, 2005, 4, 455-459.
27. L. Y. Chen, Y. T. Yin, C. H. Chen and J. W. Chiou, *J. Phys. Chem. C*, 2011, 115, 20913-20919.
28. I. Herman, J. Yeo, S. Hong, D. Lee, K. H. Nam, J. H. Choi, W. H. Hong, D. Lee, C. P. Grigoropoulos and S. H. Ko, *Nanotechnology*, 2012, 23, 194005-194009.
29. K. Sun, Y. Jing, C. Li, X. F. Zhang, R. Aguinaldo, A. Kargar, K. Madsen, K. Banu, Y. C. Zhou, Y. Bando, Z. W. Liu and D. L. Wang, *Nanoscale*, 2012, 4, 1515-1521.
30. W. Zhou, C. Cheng, J. P. Liu, Y. Y. Tay, J. Jiang, X. T. Jia, J. X. Zhang, H. Gong, H. H. Hng, T. Yu and H. J. Fan, *Adv. Funct. Mater.*, 2011, 21, 2439-2445.
31. F. E. Osterloh, *Chem. Soc. Rev.*, 2013, 42, 2294-2320.
32. M. J. Bierman and S. Jin, *Energ. Environ. Sci.*, 2009, 2, 1050-1059.
33. T. S. Arthur, D. J. Bates, N. Cirigliano, D. C. Johnson, P. Malati, J. M. Mosby, E. Perre, M. T. Rawls, A. L. Prieto and B. Dunn, *MRS Bull.*, 2011, 36, 523-531.
34. H. H. Li, Y. Y. Fu, H. X. Liu, M. Y. Zhu, Z. Peng, J. Yang, J. Li, X. Y. Huang, Y. Jiang, Q. Q. Liu, X. J. Shi, H. Wu, Y. H. Yang and Q. Liu, *Inorg. Chem. Commun.*, 2013, 30, 182-186.
35. Y. C. Qiu, K. Y. Yan, H. Deng and S. H. Yang, *Nano Lett.*, 2012, 12, 407-413.
36. O. Lupan, T. Pauporte, L. Chow, B. Viana, F. Pelle, L. K. Ono, B. R. Cuenya and H. Heinrich, *Appl. Surf. Sci.*, 2010, 256, 1895-1907.
37. K. M. McPeak, T. P. Le, N. G. Britton, Z. S. Nickolov, Y. A. Elabd and J. B. Baxter, *Langmuir*, 2011, 27, 3672-3677.
38. H. T. Nguyen, F. Yao, M. R. Zamfir, C. Biswas, K. P. So, Y. H. Lee, S. M. Kim, S. N. Cha, J. M. Kim and D. Pribat, *Adv. Energy Mater.*, 2011, 1, 1154-1161.
39. I. S. Cho, Z. B. Chen, A. J. Forman, D. R. Kim, P. M. Rao, T. F. Jaramillo and X. L. Zheng, *Nano Lett.*, 2011, 11, 4978-4984.
40. J. H. Kong, Y. F. Wei, L. P. Yang, W. A. Yee, Y. L. Dong, R. Zhou, S. Y. Wong, L. Ke, X. W. Sun, H. J. Du, X. Li and X. H. Lu, *J. Phys. Chem. C*, 2013, 117, 10106-10113.
41. A. I. Hochbaum and P. D. Yang, *Chem. Rev.*, 2010, 110, 527-546.
42. A. Wolcott, W. A. Smith, T. R. Kuykendall, Y. P. Zhao and J. Z. Zhang, *Adv. Funct. Mater.*, 2009, 19, 1849-1856.
43. K. S. Ahn, Y. Yan, S. Shet, K. Jones, T. Deutsch, J. Turner and M. Al-Jassim, *Appl. Phys. Lett.*, 2008, 93, 163117.
44. Y. F. Wei, L. Ke, J. H. Kong, H. Liu, Z. H. Jiao, X. H. Lu, H. J. Du and X. W. Sun, *Nanotechnology*, 2012, 23, 235401-235408.
45. X. Y. Yang, A. Wolcott, G. M. Wang, A. Sobo, R. C. Fitzmorris, F. Qian, J. Z. Zhang and Y. Li, *Nano Lett.*, 2009, 9, 2331-2336.
46. C. Liu, X. B. Xu, A. J. E. Rettie, C. B. Mullins and D. L. Fan, *J. Mater. Chem. A*, 2013, 1, 8111-8117.
47. B. Klahr, S. Gimenez, F. Fabregat-Santiago, T. Hamann and J. Bisquert, *J. Am. Chem. Soc.*, 2012, 134, 4294-4302.
48. A. Zaban, M. Greenshtein and J. Bisquert, *ChemPhysChem*, 2003, 4, 859-864.
49. Y. J. Lin, Y. Xu, M. T. Mayer, Z. I. Simpson, G. McMahon, S. Zhou and D. W. Wang, *J. Am. Chem. Soc.*, 2012, 134, 5508-5511.

50. J. S. Yang, W. P. Liao and J. J. Wu, *ACS Appl. Mater. Interfaces*, 2013, 5, 7425-7431.
51. X. Lu, H. J. Zhou, G. J. Salamo, Z. R. Tian and M. Xiao, *New J. Phys.*, 2012, 14, 1-10.
52. H. G. Kim, P. H. Borse, J. S. Jang, C. W. Ahn, E. D. Jeong and J. S. Lee, *Adv. Mater.*, 2011, 23, 2088-2092.
53. H. M. Chen, C. K. Chen, R. S. Liu, L. Zhang, J. Zhang and D. P. Wilkinson, *Chem. Soc. Rev.*, 2012, 41, 5654-5671.
54. S. Cho, J. W. Jang, K. J. Kong, E. S. Kim, K. H. Lee and J. S. Lee, *Adv. Funct. Mater.*, 2013, 23, 2348-2356.
55. Z. F. Wang, P. Xiao, L. Qiao, X. Q. Meng, Y. H. Zhang, X. L. Li and F. Yang, *Physica B*, 2013, 419, 51-56.
56. M. Gratzel, *Nature*, 2001, 414, 338-344.
57. B. Liu, H. M. Chen, C. Liu, S. C. Andrews, C. Hahn and P. Yang, *J. Am. Chem. Soc.*, 2013, 135, 9995-9998.
58. Y. Y. Bu, Z. Y. Chen, W. B. Li and J. Q. Yu, *ACS Appl. Mater. Interfaces*, 2013, 5, 5097-5104.
59. Z. Y. Yin, Z. Wang, Y. P. Du, X. Y. Qi, Y. Z. Huang, C. Xue and H. Zhang, *Adv. Mater.*, 2012, 24, 5374-5378.
60. X. P. Qi, G. W. She, X. Huang, T. P. Zhang, H. M. Wang, L. X. Mu and W. S. Shi, *Nanoscale*, 2014, 6, 3182-3189.